

USE OF X-RAY STAR HORIZON CROSSINGS TO ENHANCE PERFORMANCE OF X-RAY NAVIGATION

Nathaniel C. Ruhl^{*}, Andrea N. Lommen[†], Noah H. Schwab[‡], Romana M. Hladky[§],
Kent S. Wood[¶], and Paul S. Ray^{||}

A previous report (Wood et al., AAS 20-124) described the feasibility of using horizon crossings of celestial X-ray sources for satellite navigation, a technique of autonomous, on-board navigation that could complement the previously developed and tested method for X-ray pulsar navigation known as XNAV (Mitchell et al., AAS 18-155). The AAS 20-124 paper evaluates strengths and weaknesses of XNAV, and theorizes that horizon crossings could be used to gain navigational information that is complementary to XNAV. Subsequently, we have developed the Horizon Crossing Navigational Method (HCNM), which uses the same X-ray instrument that was used to perform the first real-time on-orbit demonstration of XNAV, the Neutron Star Interior Composition Explorer (NICER) telescope aboard the International Space Station (ISS). In this paper, we present preliminary results of HCNM for two NICER horizon crossings, using 1-5 keV X-rays, and explain how this technique can be used in conjunction with XNAV to perform more effective X-ray navigation near planets. Depending on the brightness of an X-ray source, HCNM can provide in-track position corrections of less than one kilometer, provided the model for X-ray absorption in the planet's atmosphere and the input orbital model are not the limiting factors. Whereas XNAV can yield precise navigational results in between planets, HCNM can yield precise results around planets. Together, these two methods can be used for accurate autonomous navigation anywhere in space throughout our Solar System and beyond.

INTRODUCTION

Excluding navigation around the Earth, Moon, and Mars, spacecraft navigation is extremely reliant on Earth-based radio and optical measurements.¹ Autonomous navigational capabilities are becoming more and more desirable, not only for long-distance science and exploration missions, but also for missions in our Solar System that require automated safe return to Earth in the event that radio-links are compromised.¹ Celestial-based navigation that uses X-ray sources has the potential to meet these needs and determine high-precision navigational information from X-ray data collected by sensors on-board the spacecraft. X-ray sources, although often variable, have reliable observational qualities that can be exploited for navigation and celestial timekeeping.² In addition to the qualities inherent in X-ray *sources*, the short X-ray *wavelengths* (~ 1 nm to 0.1 nm) present further advantages over the wavelengths of visible light and radio waves. X-rays are less affected by

^{*}Physics Student, Haverford College, Haverford, PA 19041

[†]Professor of Physics and Astronomy, Haverford College

[‡]Physics Student, Haverford College

[§]Physics Student, Haverford College

[¶]Technology Services Corporation, resident at U.S. Naval Research Laboratory

^{||}U.S. Naval Research Laboratory

absorption, scattering, and in some situations, dispersion. Because of their short wavelength, X-rays are far less subject to diffraction. As we will see in this paper, the attenuation of X-rays in planetary atmospheres is another highly predictable feature that can be used for navigational purposes. We introduce the Horizon Crossing Navigational Method (HCNM) for autonomous, celestial-based navigation around planets with atmospheres: a method that is highly complementary to existing techniques of X-ray navigation. Although autonomous optical navigation has seen substantial development, especially with the invention of the Deep Space Positioning System (DPS), optical navigation around planets requires knowledge of the planet’s topography, high definition cameras, and memory-intensive image-processing software to distinguish topographical features. On the other hand, HCNM requires knowledge of the state and composition of a planet’s atmosphere, but it is much less computationally expensive, as it does not require any knowledge of a planet’s topography.^{1,3}

Solar and stellar occultations, particularly in the ultraviolet and extreme ultraviolet passbands, have been used for many years to remotely sense the atmospheres of Earth and other planets.⁴ Different wavelengths of light penetrate different layers of a planet’s atmosphere. Since they are attenuated by different mechanisms and atmospheric species, the occultation technique provides an opportunity to gain much information about the composition and structure of the planet’s atmosphere as a function of altitude.^{5,6} During the Naval Research Laboratory’s (NRL) program in X-ray Navigation and X-ray Astronomy in the late 1900’s and early 2000’s, researchers at NRL discovered that celestial X-ray point sources are ideal candidates for planetary occultations. This is, in part, because X-rays are entirely absorbed by inner K-shell and L-shell electrons through the photoelectric effect, and therefore are absorbed in the same way by atoms and by molecules.⁴ In this way, X-ray absorption is independent of ionization state, electron state, and chemical bonds of atmospheric gases.⁴ NRL researchers also identified that rising or setting occultations, also known as horizon crossings, could be used in two ways: one in which knowledge about the satellite’s position is used in order to make atmospheric measurements, and the other in which knowledge about the planet’s atmosphere is used to determine the satellite’s position.⁷ On the atmospheric science side, the technique of X-ray Occultation Sounding (XOS) was introduced by Determan et al. (2007) to measure neutral atmospheric density at altitudes of 70 – 150 km above Earth. Recently, similar X-ray occultation techniques have been used by Katsuda et al. (2021) and Rahmati et al. (2020) to measure the atmospheric density profiles of Earth and Mars in the altitude ranges in which X-rays are transmitted.^{8,9} To our knowledge, we are the first to study X-ray horizon crossings from a navigational perspective since the NRL in the 1990’s and 2000’s, but the theoretical framework laid out by Determan and other NRL researchers has influenced our method of analysis of horizon crossings.^{4,10,11}

XNAV and HCNM: Complementary Methods of X-ray Navigation

The first real-time, on-board, and autonomous demonstration of X-ray navigation was performed aboard the International Space Station (ISS) in 2017 and 2018 in a technology demonstration named SEXTANT, The Station Explorer for X-ray Timing and Navigation Technology.² SEXTANT performed the world’s first demonstration of X-ray Pulsar Navigation (XNAV), which provides a Global Positioning System (GPS)-like navigation by exploiting the highly predictable nature of pulsars over long timescales.^{2,12} The main idea behind XNAV is that Millisecond Pulsars (MSPs) rotate at a highly stable rate (with millisecond periods), which enables them to act as extremely accurate clocks for navigation.² In this method, the time at which a pulse is expected to arrive at the solar system barycenter (SSB) is compared with the time at which the pulse is detected by an X-ray

detector aboard a spacecraft. By simultaneously comparing these times of arrivals (TOAs) for three or more pulsars, it is possible to determine the full three-dimensional position of the spacecraft with respect to the SSB. Moreover, ground-based and space-based telescopes continually update pulsar *ephemerides* and record their pulse period to high precision, which ensures the accuracy of MSP's for navigation even as their rotation slows down over long periods of time.² In 2017, XNAV was able to maintain a less-than 10 km root-sum-squared (RSS) navigation error in LEO over a period of five days.²

Horizon crossings of X-ray sources, in particular point sources such as neutron stars and black holes, can be used in conjunction with XNAV to perform more effective navigation near and around planets.¹³ XNAV does not work to its full potential for spacecraft in low-altitude orbit around planets, since orbital perturbations can cause the accuracy of an orbital propagator to degrade rapidly in low-altitude orbit, which affects the performance of pulsar timing. In this way, XNAV is more suitable for interplanetary trajectories, while horizon crossings are ideal for navigation near planets. One of the main advantages of using horizon crossings for navigation over pulsar navigation is that achievable position determination for XNAV is determined by the speed of light, c , multiplied by the accuracy in measuring pulse TOAs, δt_{toa} , while accuracy of position determination for horizon crossings is based on the accuracy in measuring the time of the horizon crossing, δt_{hc} , multiplied by the spacecraft's velocity, v .¹³ This gives horizon crossings an advantage of

$$F = \frac{c\delta t_{toa}}{v\delta t_{hc}}. \quad (1)$$

Results in this paper show that $\delta t_{hc} \approx 30$ ms can be achieved with a horizon crossing of the Crab Nebula, while $\delta t_{toa} \approx 30$ μ s is often achievable with the millisecond pulsars used by SEXTANT.¹⁴ Therefore, for spacecraft in low Earth orbit (LEO) traveling at about 7 km/sec, the ratio in Equation (1) shows that horizon crossings can be more than 43 times as accurate as XNAV. As we will see when we introduce the concept of δt_{hc} (Figure 7), the advantage can increase for horizon crossings of sources that are brighter than the Crab Nebula.¹³ Our results show that the Crab Nebula has the potential to provide in-track position measurements with a 1σ measurement uncertainty of 170 meters. We expect that a horizon crossing of Scorpius X-1, a source that is about 10 times brighter than the Crab, offers prospects of further improvement. On the other hand, the accuracy of XNAV does not have the same potential for improvement, since candidates for pulsar navigation are limited to the most predictable MSP's, which are inherently older and less bright than younger pulsars.¹⁵

HCNM and XNAV are highly complementary for two reasons 1) They can be performed with the same X-ray detector system and 2) HCNM operates where XNAV is least effective: in low-altitude orbit. XNAV performs best in deep space where measurements of pulse TOAs are unaffected by orbital accelerations, and since horizon crossings are only achievable near planets, HCNM operates where XNAV performs worst.¹³ In practice, XNAV could be used for navigation in between planets and could provide HCNM with an initial orbital solution when the spacecraft arrives at a planetary orbit. Multiple sequential horizon crossings could then be performed in order to maintain and improve an orbital description individually, or the horizon crossings could provide an additional measurement for a joint Kalman Filter with XNAV.¹³ In future missions, an X-ray detector designed in a way similar to the Neutron Star Interior Composition Explorer (NICER) has the ability to perform both XNAV and HCNM for enhanced autonomous navigation, and thus provide a seamless transition between interplanetary and orbital navigation.¹⁶ Not only can this X-ray instrument perform both HCNM and XNAV, but it also has the potential for "dual use." In addition to navigation,

X-ray horizon crossings could be performed to measure the composition and structure of an unknown planetary atmosphere. It is likely that performing and analyzing multiple sequential horizon crossings could improve both the atmospheric model and the satellite’s navigational solution at the same time.

Although NICER has the ability to perform both XNAV and HCNM, it was not originally designed to point towards Earth’s limb, which makes it very difficult to achieve successful horizon crossings. Since NICER’s star tracker is boresighted with the X-ray telescope, NICER does not have the commandable degrees of freedom to do an offset pointing.¹³ Additionally, NICER has pointing limitations due to obstructions with the ISS Express Pallet. The NICER team has worked very hard and tried many times to get the two horizon crossings presented in this paper, and we will see that one of the two is affected by a pointing error. However, if an X-ray detector is designed to point towards a planet’s limb, it is not hard for it to observe horizon crossings. As noted by Wood et al. (2020), there have been multiple X-ray experiments that have observed horizon crossings with ease.¹³ One of which is the Unconventional Stellar Aspect (USA) aboard the ARGOS satellite in 1999 – 2000, which was designed to detect horizon crossings, but since USA was mounted pointing aftward, it always observed transitions as sources were setting, not rising.^{10,13} In this way USA detected transmittance curves that start at 100% transmission and fall to 0% transmission, whereas rising horizon crossings start at 0% transmission and rise to 100%. Future space missions carrying X-ray-based avionics would be free to design for easier access to observing the horizon than NICER.

GEOMETRY OF A HORIZON CROSSING

A *rising* X-ray horizon crossing is the event where a celestial X-ray source, emerging from behind the rocky surface of a planet and over the *horizon*, comes into a spacecraft’s telescopic line of sight. The diagram in Figure 1 shows the geometry of a two-dimensional horizon crossing, where the direction vector to the source \hat{s} , is projected into the plane of the orbit as \hat{s}_{proj} . Because of NICER’s limited field of regard aboard the ISS, NICER can only observe a horizon crossing of a source that is at most 5° out of the orbital plane, but for a different instrument and spacecraft, the upper bound of the out-of-plane angle could be closer to 20° or 30° depending on orbital altitude and the radius of the orbited planet.¹³

We use this two-dimensional geometry in order to identify approximately where a horizon crossing will occur in three-dimensional space, given an orbital model and a source location. Simple geometric formulas that use the vector pole of the orbit, \hat{h} , and the direction vector to the X-ray source projected into the orbital plane, \hat{s}_{proj} , predict the location at which the two-dimensional horizon crossing starts, the position vector $\mathbf{r}_{0,2d}$. However, if the X-ray source is out of the orbital plane, it is necessary to define $\mathbf{r}_{0,3d}$, or just \mathbf{r}_0 , which is the true position at which the satellite’s line of sight (pointing to \hat{s}) is tangent to the planet’s surface. If the orbited planet had no atmosphere, full emission from the source would be detected at the position \mathbf{r}_0 , but for planets with atmospheres, a telescope observing a horizon crossing will detect higher energy photons earlier in time than lower energy photons, since higher energy photons are more likely to penetrate the denser, lower sections of the atmosphere (Figures 2 and 3). Knowing the model of a planet’s atmosphere enables the prediction of the transmittance curves that an X-ray detector will see as it emerges over the planet’s horizon, which is how we propose to use horizon crossings for navigation. By comparing the expected transmittance curve to the data collected by an X-ray detector, we can determine navigational information for the spacecraft at the position labelled \mathbf{r}_0 in Figure 1.

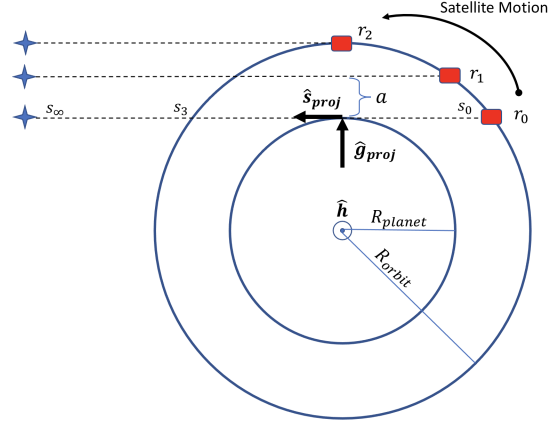


Figure 1: Two-Dimensional Geometry of a Horizon Crossing. Since the source is so far away, the direction vector to the source stays constant throughout the horizon crossing, which is shown by the parallel lines of sight at the points r_0 , r_1 , and r_2 . The “tangent altitude” of a telescopic line of sight is labeled a in the diagram and the pole of the orbit is labeled \hat{h} .

TWO NICER HORIZON CROSSINGS

We have tested and verified HCNM using two horizon crossings detected by NICER. The NICER-detected horizon crossings of the black hole binary V4641 Sagittarii (V4641 Sgr) and the Crab Nebula are shown in Figures 2 and 3 below. V4641 Sgr comprises a black hole in a binary orbit with a high mass companion star. In an active state, the black hole is luminous in X-rays because it accretes mass from its companion star. V4641 Sgr is about 20 times fainter than the Crab Nebula, although its brightness is comparable to pulsar at the center of the Crab. It is a point source with an angular diameter much less than one arc second.¹³ Point sources have always been desired for atmospheric occultations, as their rays of light are not spread into a wide cone when they penetrate the atmosphere.⁶ This enables determination of atmospheric structure and temperature on a fine scale of altitude and latitude from the remote sensing perspective, and precise in-track measurements from the navigational perspective.^{6, 13}

The Crab Nebula, on the other hand, is not binary system. It has a young, solitary neutron star at its center, which is the remnant of a supernova that took place in 1054 AD. In addition to spinning at a period of $33 \mu\text{s}$, the neutron star (pulsar) puts out a wind of high energy particles that power the surrounding Nebula. The Crab Pulsar plus the Crab Nebula together constitute a source of finite angular extent, which is about one arc-minute in X-rays. The X-ray angular extent of the Nebula is smaller than in optical or radio wavelengths, and for the purposes of this paper, it is treated as a point source. Wood et al. (2020) provides a detailed discussion of X-ray sources that can be used for horizon crossings, as well as the technical and astrophysical requirements necessary to consider when planning a NICER horizon crossing.¹³

As stated previously, the curves that overlay the data points in Figures 2 and 3 were not fit at all, but rather we used an atmospheric model of Earth to predict the transmittance curves on a scale from zero to one, and then scaled them by the *unattenuated* number of X-ray counts (the plateau at the top of a transmittance curve). The next section explains how we use a known atmospheric

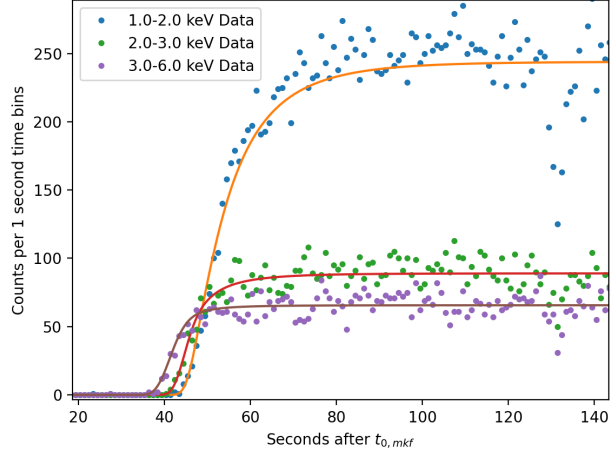


Figure 2: NICER-detected horizon crossing of V4641 Sgr on February 3, 2020. The data points are X-ray photon counts binned at one second intervals and the curves represent what we expect a horizon crossing to look like based on our atmospheric model.

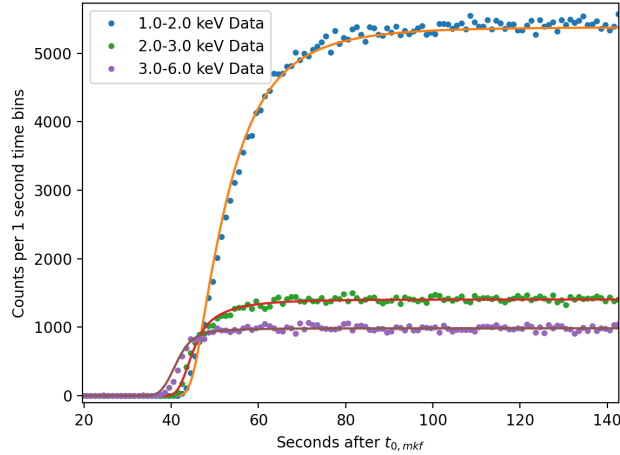


Figure 3: NICER-detected horizon crossing of the Crab Nebula on August 8, 2021.

model to predict X-ray transmittance curves.

MODELING X-RAY ATTENUATION IN PLANETARY ATMOSPHERES

In order to predict the transmission of X-rays through a planet's atmosphere, we must know its total mass attenuation coefficient. For an atmosphere with n atomic constituents, the total mass attenuation coefficient is defined as

$$\sigma(E) = \sum_n C_n \sigma_n(E) \quad (2)$$

where C_n is the relative abundance, or the *mixing ratio*, of each constituent. As discussed in the Introduction, X-ray attenuation is simple to model in a planetary atmosphere because it is solely due to absorption of photons by the innermost and most tightly bound K- and L-shell electrons. Therefore, the mass attenuation coefficient for soft X-rays is approximately equal to the photoelectric (or photoabsorption) mass attenuation coefficient, $\sigma(E) = \sigma_{pe}(E)$, since the ratio of particle size to X-ray wavelength is such that the contributions from incoherent (Compton) scattering and coherent (Rayleigh) scattering are negligible. Moving forward in this paper, we will use the term “cross section” instead of mass attenuation coefficient. We use photoelectric cross section functional fits for individual elements created by Balucinska-Church and McCammon (1992) in our model of X-ray absorption.¹⁷ These functional fits agree highly with the total mass attenuation coefficients (referred to as μ/ρ) in the National Institute of Standards and Technology (NIST) XCOM database.¹⁸ Moreover, the cross sections (cm^2/g) are nearly identical for the atomic and molecular forms of nitrogen and oxygen.¹⁷ Cross sections do change in the case of *complete ionization*,¹⁷ but this does not happen to nitrogen, oxygen, or argon in the temperature ranges of Earth’s atmosphere. These functional fits also offer the possibility to easily alter the mixing ratios in an atmosphere, which we will consider in the Section “Performance of HCNM with Uncertainties in an Atmospheric Model.”

In our definition of the total atmospheric cross section, $\sigma(E)$ (Equation (2)), we use an atmospheric mix of 78% nitrogen, 21% oxygen, and 1% argon. As noted by Determan et al. (2007), hydrogen and helium do not provide a significant contribution to atmospheric absorption because of their small cross sections and low mixing ratios in the atmosphere.⁴ Moreover, since the X-ray cross section of Ar is almost an order of magnitude larger than that of N and O above its k-edge at 3.2 keV, it plays an important role in atmospheric absorption, despite its small abundance.^{4*}

Modeling X-ray attenuation also requires a model of atmospheric density as a function of altitude, $\rho(z)$, for which we use the NRL MSISE-00 model.^{19,20} The normalized intensity, or *transmittance*, of X-rays (in a certain energy band, E) that make it through the atmosphere and is detected by the telescope is then described by Beer’s Law:

$$T(E) = e^{-\tau(E)}. \quad (3)$$

The value of $\tau(E)$, the non-dimensional optical depth, is determined by integrating the product of atmospheric density and cross section along the telescopic line of sight, and represents a measure of atmospheric transparency.⁴ The exact optical depth of the line of sight of a telescope (in orbit) to a source, a *limb-looking* geometry, is given by the integral in Equation (4):

$$\tau(E) = \int_{LOS} \sigma(E) \rho(z) ds \quad (4)$$

where ds is an infinitesimal step along the line of sight (LOS) and z is the radial altitude from Earth’s surface to a point on the line of sight. The units of $\sigma(E)$, $\rho(z)$, and ds must be chosen so that $\tau(E)$ is dimensionless. In our formulation of Beer’s law, the cross section $\sigma(E)$ is in units of cm^2/g , the mass density $\rho(z)$ is in g/cm^3 , and ds is in cm. Additionally, in order to better predict transmittance curves, we use a source’s energy spectrum as a normalized probability density function. This method enables us to better predict the shape of a transmittance curve for an energy

*A molecule’s k-edge is defined as the energy required to emit a K-shell electron, which are the innermost and most tightly bounded electrons.

band, and it is particularly important below 3 keV where value of $\sigma(E)$ can change significantly within a given energy band. We calculate a *total effective transmittance*, which is defined as

$$T_{eff} = \sum_i P(E_i)T(\sigma(E_i)), \quad (5)$$

where i represents the center of a 0.2 keV step within the desired energy band and $P(E_i)$ is equal to the area under the source's normalized spectrum in the energy range E_i , such that

$$\sum_i P(E_i) = 1. \quad (6)$$

The spectrum that is used to define $P(E_i)$ is the spectrum (in units of counts versus energy) detected by NICER during ~ 200 second time period in which the source is unattenuated by the atmosphere. Therefore, the spectrum that we use is actually the source's true spectrum convolved with NICER's response matrix.

This model of X-ray absorption enables us to predict the transmittance of X-rays over the time period of the horizon crossing, but we can also plot transmittance as a function of the tangent altitude of the telescopic line of sight, which is the point of closest approach to the planet. Tangent altitude, which is labeled a in Figure 1, is fundamental when measuring atmospheric density from a horizon crossing, since the atmosphere is most dense at the tangent point on the line of sight.^{4,8} Plotting transmittance as a function of tangent altitude normalizes geometric and temporal differences from different horizon crossings. In other words, plots of transmittance versus tangent altitude are identical among crossings, provided the atmosphere is unchanged. Figure 4 shows transmittance versus tangent altitude of the telescopic line of sight, calculated for the observation of V4641 Sgr.

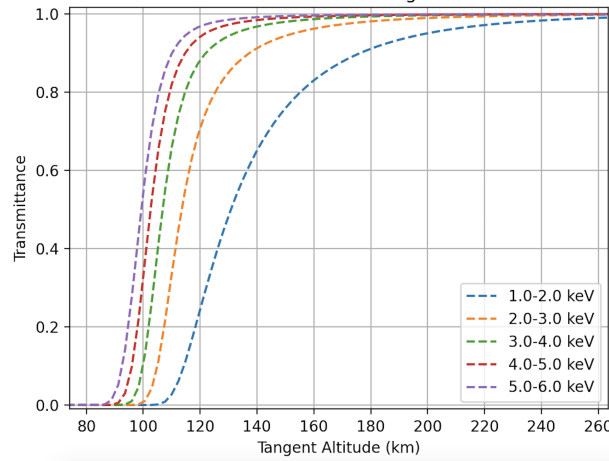


Figure 4: Predicted transmittance of X-rays versus tangent altitude above Earth. The curves show that higher energy X-rays can penetrate lower portions of Earth's atmosphere, but the lower energies are not detected until the telescope's line of sight goes through a higher, less dense portion of atmosphere. The transmittance curves are calculated for an atmospheric make-up of 78% nitrogen, 21% oxygen, and 1% argon, as well as a model of atmospheric mass density corresponding to the solar flux and geomagnetic activity on February 3rd, 2020. The orbital solution of the ISS during the horizon crossing of V4641 Sgr was used when calculating these models.

NAVIGATIONAL INFORMATION FROM HORIZON CROSSINGS

The goal of HCNM is to identify the time t_0 at which the satellite is at position \mathbf{r}_0 (Figure 1). HCNM has the potential to operate independently if multiple sequential horizon crossings are performed, or it can provide an input to a navigational filter whenever a horizon crossing is performed. In each scenario, it is necessary to know at least the equivalent of the geometric description of the orbit *a priori* as well as the X-ray star’s location in the sky, and we expect that it will also be important to have a good model of orbital velocity during the horizon crossing for a non-circular orbit. In the application of HCNM to a circular orbit where in-track position is not well-defined or not known at all, we must know at least the unit vector pole of the orbit, $\hat{\mathbf{h}}$, and the orbital period. In this way, we know the right ascension of the ascending node, the inclination of the orbit, and that the argument of periapsis is equal to zero. One horizon crossing is enough to completely connect the geometric description of the circular orbit to a temporal description. In the case of an elliptical orbit, two or more horizon crossings could be conducted throughout an orbit in order to fully describe the ellipse. In order to evaluate the performance of our atmospheric model and reduce uncertainty from the input orbital model, in this paper, we use position data from NICER’s GPS receiver (which is located in a file with a “.mkf” extension, and thus why we use the “mkf” subscript on mathematical symbols).

In-track Position

HCNM provides a direct measurement of in-track position by comparing the model transmittance curve to the data collected on-board the spacecraft. We expect that if the orbital velocity and cross-track position of the satellite are well-defined during the horizon crossing, HCNM will always be able to provide accurate in-track measurements. In future work, we will conduct simulations in order to understand exactly how well-defined the input orbital model (in terms of velocity and cross-track position) needs to be such that HCNM still provides accurate in-track corrections. An incorrect orbital velocity will be very important since the altitude of a point on a telescopic line of sight, and thus the atmospheric density at that point, will be incorrect and lead to an erroneous transmittance model. Moreover, it is important to know the satellite’s cross-track position, or alternatively the out-of-plane angle of the source, since the telescopic line of sight would also go through different atmospheric columns with slightly different optical depths, but we expect this to be less important than orbital velocity. On the other hand, we do not expect the radial position of the input orbital model to be crucial. As can be seen in Figure 1, altering the radial coordinate of the satellite (on a scale of 10’s of kilometers) only increases the length of the line of sight through a very thin atmosphere at the altitude of the orbit, and thus it should not affect the prediction of a transmittance curve very much.

After calculating the model transmittance curve for a certain energy range, we then scale the model by the number of unattenuated counts detected at the top of the data transmittance curve (Figure 5), and numerically slide the model across the data. At every point in time within the slide, we calculate a value of χ^2 between the model and the data points in the range of 1% to 99% transmission (Figure 5). χ^2 is given in the following formula:

$$\chi^2 = \sum_i \frac{(O_i - E_i)^2}{E_i^2} \quad (7)$$

where O_i is the number of observed counts in the i ’th time bin and E_i is the number of expected

counts. Minimizing χ^2 identifies the value of $t_{0,e}$, the origin of Figure 5 and the time at which the horizon crossing and atmospheric model predicts that the ISS is at the position \mathbf{r}_0 .

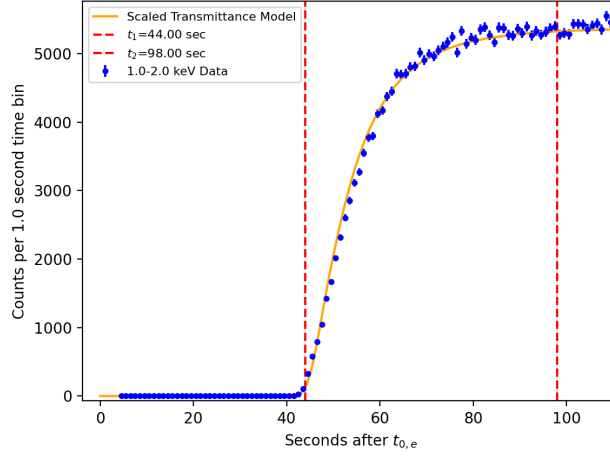


Figure 5: The scaled model transmittance curve is compared to data in the range of 1% to 99% transmission.

As can be seen near the origin of the plot in Figure 5, the X-ray data for the first 4 seconds of the Crab Nebula horizon crossing was filtered out through standard pre-processing of NICER data. This is because NICER’s pointing vector was not yet locked onto the Crab. Even though NICER was not locked on to the source when it crossed the hard-rock *Earth horizon*, it still had time to correct its pointing control before reaching the *X-ray horizon* and observe a full horizon crossing. Nevertheless, we will see that NICER’s pointing error at the beginning of the crossing does affect the results for the Crab Nebula, and specifically, it affects the upper energy bands, which are detected earlier in time than the lower energy bands. As shown in Figure 6, which shows the right ascension (RA) and declination (DEC) of NICER’s “look direction” in the sky as compared to the fixed position of the Crab Nebula, NICER is not locked onto the Crab Nebula for the first 40 seconds of the horizon crossing. In the horizon crossing of V4641 Sgr, NICER is locked on the entire time. The pointing error during the Crab observation has a disproportionate affect on the detection of high energy X-rays, which start to get detected before 40 seconds. At 40 seconds, NICER is only ~ 0.5 arc minutes away from the Crab Nebula, which has an angular extent in X-rays of about one arc minute. Although the pointing error at 40 seconds is relatively small, we expect that the finite angular extent of the Crab Nebula and NICER’s smaller effective area at higher energies may accentuate the error. Additionally, if the Crab Pulsar were not in NICER’s field of view at 40 seconds, the X-ray flux detected by NICER could decrease by 10%. We are currently working to quantitatively describe the decrease in X-ray flux detected by NICER at the beginning of the horizon crossing.

In order to understand the results tables for the horizon crossings, we must first define relevant quantities. The time $t_{0,mkf}$ is the exact time at which the ISS is at the position $\mathbf{r}_{0,mkf}$, and $t_{0,e}$ is the time at which the horizon crossing predicts that the ISS is at the position $\mathbf{r}_{0,mkf}$. The subscript “e” denotes that the value of $t_{0,e}$ is specific for the energy band used in the analysis. Table 7 and Table 8 in Appendices A and B show the values of $t_{0,mkf}$ and $\mathbf{r}_{0,mkf}$. The error in the in-track position, Δr_{hc} , is calculated by multiplying the velocity of the ISS at $\mathbf{r}_{0,mkf}$ by the error in identifying

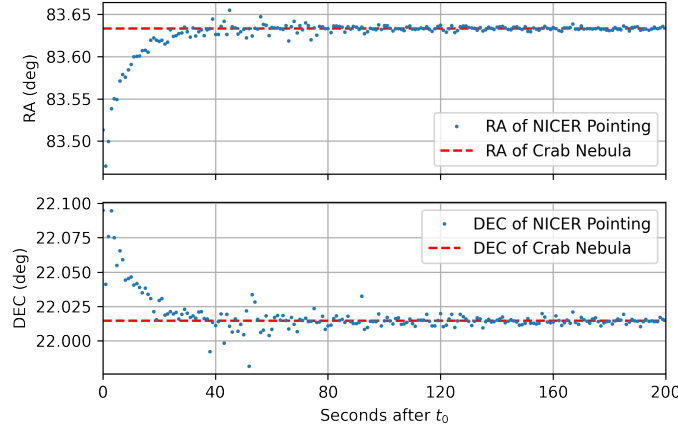


Figure 6: Right ascension (RA) and Declination (DEC) of NICER’s “look direction” in the sky. NICER locks onto the Crab Nebula after the first 40 seconds of the horizon crossing.

$t_{0,mkf}$, which we define as Δt_{hc} :

$$\Delta r_{hc} = |\mathbf{v}_{0,mkf}| \cdot \Delta t_{hc} \quad (8)$$

$$\Delta t_{hc} = t_{0,mkf} - t_{0,e}. \quad (9)$$

As can be seen in Figure 5, each data point has an error bar of \sqrt{N} where N is the number of X-ray photon counts in a one second time bin. In order to estimate the error related to the Poisson statistics involved in binning photon events, we quote a standard error for $t_{0,e}$, the best-aligned value of t_0 for a specific energy band. The standard error δt_{hc} represents the amount of time required for the values of χ^2 to increase by one when sliding the model over the data, from either side of the minimum χ^2 value at $t_{0,e}$. Assuming that the error in identifying $t_{0,mkf}$ is much smaller than the error in identifying $t_{0,e}$, the uncertainty associated with Δt_{hc} is equal to δt_{hc} . (For the sake of showing δt_{hc} , an important quantity related to source brightness, in the results tables, we will not consider the uncertainty in $t_{0,mkf}$, although it should be defined by the accuracy of the “mkf” positions and the 0.01 second time-steps used to interpolate the “mkf” data. Because of NICER’s high-precision pulsar timing, we expect the error in the “mkf” positions to be ≤ 300 meters). The value of Δr_{hc} thus has a standard error equal to

$$\delta r_{hc} = |\mathbf{v}_{0,mkf}| \cdot \delta t_{hc}. \quad (10)$$

Table 1 and Table 2 below show the results of HCNM for the two horizon crossings. Figure 7 shows that the $\chi^2 + 1$ standard errors, the values of δt_{hc} , are inversely proportional to $\sqrt{N_0}$, where N_0 is the number of unattenuated counts (the number of photon counts at the top of a transmittance curve of a given energy, unattenuated by the atmosphere). Since we use the GPS position as our input orbital model, we can assume that Δt_{hc} is for the most part, caused by imperfections in our atmospheric model. Therefore, these results enable us to directly evaluate the performance of our relatively simplistic atmospheric model for Earth. Specifically, the value Δt_{hc} is defined such that when $\Delta t_{hc} > 0$, our atmospheric model is “thicker” than Earth’s real atmosphere as indicated by

the data, and when $\Delta t_{hc} < 0$, our model is too transparent. This concept will be revisited in the discussion of Tables 1 and 2, as well as the section “Performance of HCNM with Uncertainties in an Atmospheric Model.”

Table 1: Results from the horizon crossing of V4641 Sgr. Δt_{hc} is the error in correctly identifying $t_{0,mkf}$, the time at which the spacecraft is at the position $\mathbf{r}_{0,mkf}$. Δr_{hc} is the in-track error corresponding to Δt_{hc} . The uncertainties δt_{hc} and δr_{hc} are related to the number of unattenuated counts in a given energy band (Figure 7).

Energy Band	1.0 – 2.0 keV	2.0 – 3.0 keV	3.0 – 4.0 keV	4.0 – 5.0 keV
$\Delta t_{hc} \pm \delta t_{hc}$ (sec)	0.02 ± 0.14	0.11 ± 0.20	0.27 ± 0.27	0.02 ± 0.38
$\Delta r_{hc} \pm \delta r_{hc}$ (km)	0.15 ± 1.09	0.84 ± 1.54	2.07 ± 2.09	0.15 ± 2.90
Unattenuated Counts, N_0	244	89	40	19

Table 2: Initial results from the horizon crossing of the Crab Nebula when comparing all curves in the time range that corresponds to 1% – 99% transmission.

Energy Band	1.0 – 2.0 keV	2.0 – 3.0 keV	3.0 – 4.0 keV	4.0 – 5.0 keV
$\Delta t_{hc} \pm \delta t_{hc}$ (sec)	0.01 ± 0.03	-0.06 ± 0.05	-0.41 ± 0.07	-0.66 ± 0.09
$\Delta r_{hc} \pm \delta r_{hc}$ (km)	0.08 ± 0.20	-0.46 ± 0.41	-3.14 ± 0.54	-5.05 ± 0.72
Unattenuated Counts, N_0	5378	1406	584	275

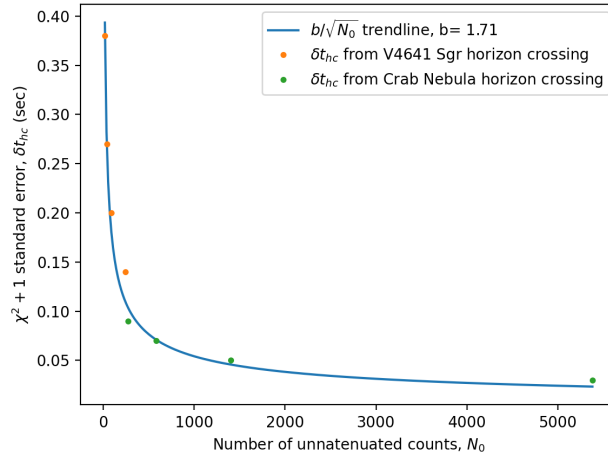


Figure 7: Values of δt_{hc} plotted against N_0 from both NICER horizon crossings (Tables 1 and 2). The standard error δt_{hc} represents the amount of time required for the values of χ^2 to increase by one when comparing the scaled model transmittance curve to the X-ray data. The temporal errors δt_{hc} should be multiplied by orbital velocity (~ 7.6 km/s) to get positional errors, δr_{hc} .

Results for V4641 Sgr in Table 1 show in-track position errors that agree with zero to one standard error for all energy bands. We also see that argon’s k-edge at 3.2 keV may affect the reliability of the 3.0 – 4.0 keV energy band, which is the energy band with the largest error in the horizon crossing of

V4641 Sgr.* In-track errors for the Crab Nebula horizon crossing shown in Table 2 agree with zero at slightly above one standard error for the energy bands from 1.0 – 3.0 keV and show a systematic error above 3.0 keV. We expect that negative values of Δt_{hc} are caused by NICER’s pointing error during the first 40 seconds of the crossing, and we expect that this pointing error may also amplify the effects of the non-point source nature of the Crab Nebula. Specifically, when NICER is not locked-on and/or does not observe the full intensity of the Crab Nebula, the transmittance data starts to rise at a slightly later time than we expect. As shown in Figure 8, this distorts the shape of the transmittance data as compared to the model curve. Additionally, the pointing error leads to an increase in X-ray background noise during the first 40 seconds, but the relatively small background rate detected by NICER should not affect the performance of HCNM unless the source is extremely dim.

Correcting NICER’s Pointing Error

In spite of NICER’s late lock, it is still possible to obtain accurate information by using the portion of the data curve that it not affected by the pointing error, instead of using the full 1% to 99% transmittance range used in Figure 5. Based on the model transmittance curve for 4.0-5.0 keV, we expect to see about 36.5% transmission at 40 seconds after $t_{0,mkf}$ and 51.7% at 41 seconds. We can thus compare the model to the data within the range of 36.5% – 99.0% or 51.7% – 99.0% for a better comparison. Figure 8 and Figure 9 show the curve comparisons when using the two restricted comparison ranges, and Table 3 shows the results of each.

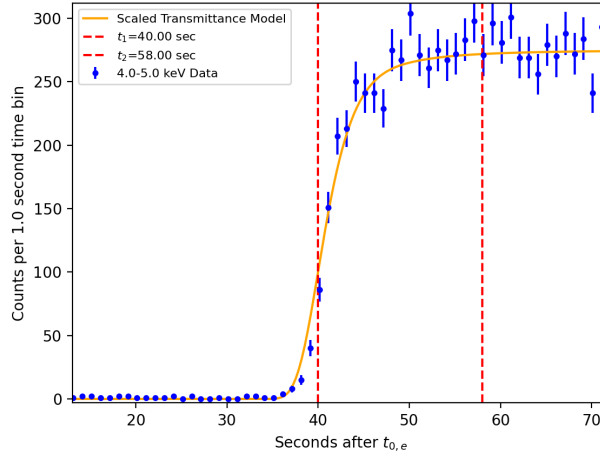


Figure 8: Horizon crossing of the Crab Nebula where the model is compared to data in a restricted time range. The shape of the data curve is distorted by delayed lock-on of the attitude control at times less than ~ 40 seconds. The comparison in the range of 40.0 – 58.0 seconds includes 18 data bins, the first of which is affected by NICER’s late lock.

The comparison from 40.0 – 58.0 seconds is still negatively affected by the pointing error, while the 41.0 – 58.0 second comparison achieves $\Delta t_{hc} < \delta t_{hc}$. As shown in Figure 8, the comparison range that starts at 40.0 seconds includes a data bin centered at 40.1 seconds, and therefore X-ray

*In addition to argon’s k-edge at 3.2 keV, nitrogen and oxygen have k-edges at 0.41 keV and 0.54 keV respectively, which will affect the reliability of energy bands below 0.6 keV.

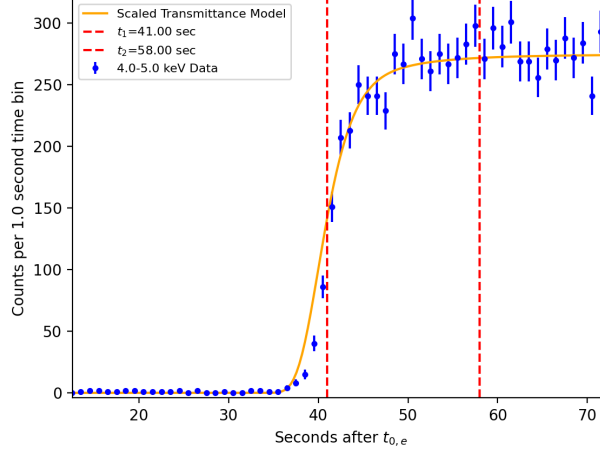


Figure 9: Horizon crossing of the Crab Nebula where the model is compared to data in a restricted time range. The shape of the data curve is distorted by delayed lock-on of the attitude control at times less than ~ 40 seconds. The comparison in the range of 41.0 – 58.0 seconds includes 17 data bins that are unaffected by NICER’s late lock.

Table 3: HCNM results for the 4.0 – 5.0 keV energy band in the Crab Nebula horizon crossing.

Time Range	40.0 – 58.0 seconds	41.0 – 58.0 seconds
Transmittance Range	36.5% – 99.0%	51.6% – 99.0%
$\Delta t_{hc} \pm \delta t_{hc}$ (sec)	-0.39 ± 0.16	-0.01 ± 0.25
$\Delta r_{hc} \pm \delta r_{hc}$ (km)	-2.98 ± 1.21	-0.08 ± 1.88

events from 39.6 – 40.6 seconds are included. This means that the data point at 40.1 seconds may also be affected by NICER’s late lock onto the Crab, which occurs at ~ 40.0 seconds. On the other hand, the first data bin in the 41.0 – 58.0 second range does not seem to be affected at all by NICER’s late lock, since it only contains data from after 40.6 seconds. It is also important to note that the value of δt_{hc} is considerably larger for the 41.0 – 58.0 second comparison range. Since one less data point is used in the comparison when we restrict the time range from starting at 40 seconds to starting at 41 seconds, which increases the statistical uncertainty of the comparison. Therefore, δt_{hc} is smaller for the shorter comparison window, even though the over fit is better. Values of δt_{hc} for both shortened comparison ranges are larger than $\delta t_{hc} = 0.09$ seconds in the 1% – 99% transmittance comparison in Table 2. Not only is our method of estimating uncertainty with δt_{hc} strongly related to source brightness, but it is also related to the number of data points involved in the comparison.

The 2.0 – 3.0 keV and 3.0 – 4.0 keV energy bands are also affected by NICER’s pointing error in a similar way as the 4.0 – 5.0 keV energy band, but their improvements are less pronounced, since smaller portions of their curves are affected by the pointing error Table 4. The 1.0 – 2.0 keV data is unaffected by the pointing error, as it does not begin to rise until ~ 43 seconds after $t_{0,mkf}$. The counts in this energy band rise later in time because lower energy photons cannot penetrate as deeply in the atmosphere as the higher energies. HCNM results for all energy bands in the Crab horizon crossing are shown in Table 4, and this time, only the most reliable portion of the data is

used in our analysis. Excluding the 1.0 – 2.0 keV energy band which uses the same 1.0% – 99.0% transmission range as used in Table 2, each comparison range starts at 41.0 seconds and ends when the model transmittance curve reaches 99.0%. Because of the restricted comparison window, the values of δt_{hc} are larger than the values in Table 2.

Table 4: Results for the horizon crossing of the Crab Nebula when comparing only the portions of the data when NICER is confidently locked-on.

Energy Band	1.0 – 2.0 keV	2.0 – 3.0 keV	3.0 – 4.0 keV	4.0 – 5.0 keV
Time Range	44.0 – 98.0 sec	41.0 – 76.0 sec	41.0 – 65.0 sec	41.0 – 58.0 sec
Transmittance Range	1.0% – 99.0%	3.8% – 99.0%	25.6% – 99.0%	51.6% – 99.0%
$\Delta t_{hc} \pm \delta t_{hc}$ (sec)	0.01 ± 0.03	0.04 ± 0.05	-0.24 ± 0.10	-0.01 ± 0.25
$\Delta r_{hc} \pm \delta r_{hc}$ (km)	0.08 ± 0.20	0.31 ± 0.40	-1.84 ± 0.77	-0.08 ± 1.88

Weighted Mean of Four Energy Bands

In order to determine the most accurate in-track correction from a horizon crossing, we can take the weighted mean of the results from the four energy bands. In practice, this is a method of combining the four results of $t_{0,e} \pm \delta t_{0,e}$ into a single value of $t_0 \pm \delta t_0$ which will, from a statistical perspective, always be more accurate. This value of t_0 could then be input into a navigational filter with a measurement uncertainty of δt_0 . In this paper, We will calculate the weighted means of Δt_{hc} and Δr_{hc} in order to determine the overall in-track accuracy attainable using V4641 Sgr. and the Crab Nebula. The weights for each energy band are proportional to $1/\delta t_{hc}^2$ and $1/\delta r_{hc}^2$, which are then normalized to sum to unity. The resulting values of Δt_{hc} , Δr_{hc} , and their corresponding uncertainties are shown in Table 5. These weighted means quantify overall in-track temporal and positional accuracy achieved from the horizon crossing V4641 Sgr. and the adjusted (i.e., “trimmed”) horizon crossing of the Crab Nebula.

Table 5: Overall results for the Horizon Crossings of V4641 Sgr. and the Crab Nebula. This table shows the weighted mean values of Δt_{hc} and Δr_{hc} from Table 1 and Table 4, as well as their corresponding uncertainties.

Weighted Mean	V4641 Sgr.	Crab Nebula
$\Delta t_{hc} \pm \delta t_{hc}$	0.08 ± 0.10 sec	0.002 ± 0.025 sec
$\Delta r_{hc} \pm \delta r_{hc}$	600 ± 800 m	24 ± 170 m

Discussion of Atmospheric Cross Section

In our atmospheric model, we use the average volumetric mix of Earth’s atmosphere below 85 km to determine $\sigma(E)$: 78% N₂, 21% O₂, 1% Ar. While these ratios change with altitude above 85 km and there are other trace molecules in the upper atmosphere, our results show that this simple ratio is enough to achieve sub-kilometer in-track position determinations. Nevertheless, the atmospheric model presented in this paper could possibly be made more robust by making the atmospheric mix a function of altitude, including hydrogen and helium in the mix, or even by considering other thermospheric phenomena, but even with this simplistic atmospheric model, $\Delta t_{hc} \leq \delta t_{hc}$ for all but one energy band. Continuing to improve Earth’s atmospheric model would even enable HCNM to provide in-track corrections for satellites in LEO, but for the case of deep space navigation, the goal is to use the simplest atmospheric model possible that will still produce accurate results.

We will explore one of these *limiting case* scenarios in the Section “Performance of HCNM with Uncertainties in an Atmospheric Model”.

Other Navigational Information From HCNM

Horizon crossings also offer the opportunity to gain information about a satellite’s orbital period. If the X-ray detector is used in a manner similar to a *transit telescope* used in astronomy and celestial navigation at sea, and the source is detected as it appears from behind the planet’s shadow during multiple orbits, an estimate of orbital period can be determined. The estimate of orbital period should get better and better with each orbit. Additionally, the horizon crossing transmittance curves may be able to provide cross-track information, which would come in the form of specifying the out-of-plane angle of the source, and thus provide a correction to the orbital pole vector. We also expect that the geometry presented in Figure 1 may offer the opportunity to determine an instantaneous radial position at the time of crossing, t_0 . Each of these methods are still being developed.

PERFORMANCE OF HCNM WITH UNCERTAINTIES IN AN ATMOSPHERIC MODEL

In order to evaluate the importance of correctly identifying the total effective cross section, $\sigma(E)$, of a planetary atmosphere, we will consider the 1.0 – 2.0 keV energy band from the horizon crossing of the Crab Nebula. The 1.0 – 2.0 keV band is unaffected by NICER’s pointing error and has a much smaller standard error than any of the energy bands in the V4641 Sgr horizon crossing, enabling us to more easily see significant trends. This is a hypothetical exercise used to demonstrate how our model of X-ray transmittance behaves when the model for $\sigma(E)$ contains uncertainty. In this analysis, we remove the summation in Equation (2), the total effective atmospheric cross section, and use the same MSISE-00 density profile as in the previous analyses. Therefore, this analysis shows the accuracy attainable with HCNM when there is significant uncertainty in atmospheric composition. The results in Table 6 show the performance of HCNM when using $\sigma(E) = 0.78\sigma_N(E) + 0.21\sigma_O(E) + 0.01\sigma_{Ar}(E)$ (same result as Table 4), as well as when using the approximations that $\sigma(E) = \sigma_N(E)$ and $\sigma(E) = \sigma_O(E)$. For the 1.0 – 2.0 keV band, the pure nitrogen cross section is $\sim 7\%$ smaller than the expected three-element mix, while the pure oxygen cross section is $\sim 30\%$ larger. As previously stated, photoelectric cross sections are equal for atoms and molecules, so we simply refer to the elemental symbols of N and O in Figure 10 and Table 6.

Table 6: Results for the 1.0 – 2.0 keV energy band from the horizon crossing of the the Crab Nebula when the mixing ratio of $\sigma(E)$ is uncertain. The same model of mass density, $\rho(z)$, is used in each scenario.

$\sigma(E)$ Mixing Ratios	78% N, 21% O, 1% Ar	100% N	100% O
$\Delta t_{hc} \pm \delta t_{hc}$ (sec)	0.01 ± 0.03	-0.26 ± 0.03	1.11 ± 0.03
$\Delta r_{hc} \pm \delta r_{hc}$ (km)	0.08 ± 0.20	-1.99 ± 0.20	8.50 ± 0.20

As shown in Figure 10 and Table 6, both the pure nitrogen and the pure oxygen atmospheres introduce detectable systematic errors, and the case that uses $\sigma(E) = \sigma_N(E)$ is closer to the expected three-element mix than the $\sigma(E) = \sigma_O(E)$ case. Since the cross section of oxygen is larger than that of nitrogen, the direction of the errors in identifying $t_{0,mkf}$, which is indicated by the sign of Δt_{hc} , agrees with theoretical expectation. The 100% oxygen cross section produces a model atmosphere that is significantly “thicker” than the Earth’s approximate atmospheric mix with three constituents, while the atmosphere with a 100% nitrogen cross section is slightly “thinner”. As

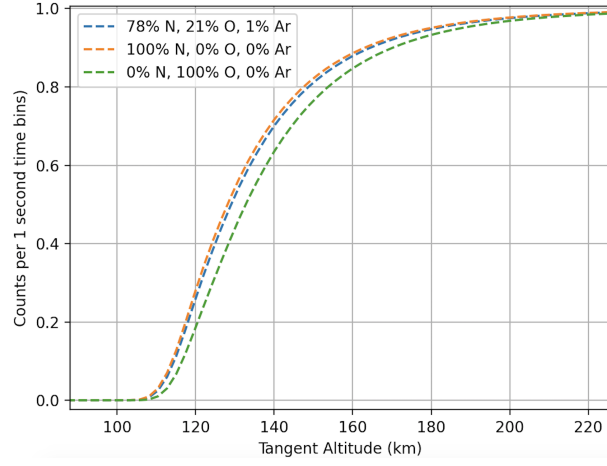


Figure 10: Model X-ray transmittance curves for different values of photoelectric cross section, $\sigma(E)$, in Earth's atmosphere. Models are calculated for the 1.0 – 2.0 keV energy band of Crab Nebula horizon crossing, and the plots correspond to three different definitions of $\sigma(E)$, $\sigma(E) = 0.78\sigma_N(E) + 0.21\sigma_O(E) + 0.01\sigma_{Ar}(E)$, $\sigma(E) = \sigma_N(E)$, and $\sigma(E) = \sigma_O(E)$, all of which use the same well-defined model for atmospheric density.

shown in Figure 11, the ratio of the cross section of oxygen to that of nitrogen increases as a function of energy. Therefore, the relative accuracy when using the single-species approximation for cross sections in Earth's atmosphere will be best for the 1.0 – 2.0 keV energy band and, in general, worse for larger energy bands.

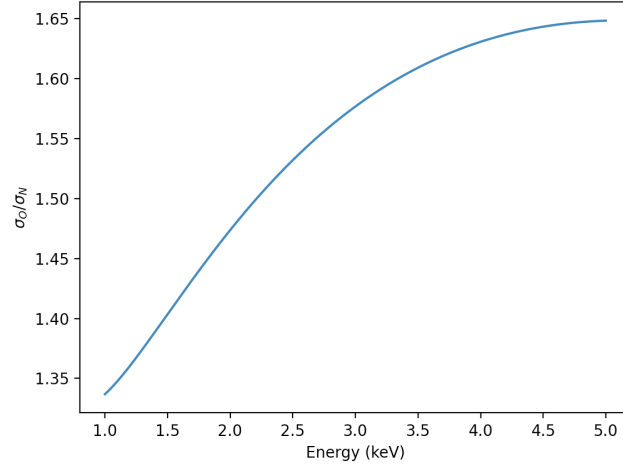


Figure 11: Ratio of the photoelectric cross section of oxygen to that of nitrogen, σ_O/σ_N , plotted against energy. Photoelectric cross section fits from Balucinska-Church and McCammon (1992) are used to make this plot.¹⁷

The analysis presented here is just the beginning of an in-depth analysis that is required to fully understand the performance of HCNM in a deep space navigational scenario. In future research, we will continue to analyze the performance of HCNM when there is uncertainty in an atmospheric model, as well as uncertainty in the input orbital model; however, the results presented here provide a starting point to understanding exactly how much must be known about a planet's atmosphere in

order for HCNM to provide reliable in-track corrections.

CONCLUSION

X-ray sources and X-ray photons exhibit predictable and reliable qualities that can be used for autonomous navigation in space. Where XNAV takes advantage of the periodicity of pulsars for navigation, HCNM exploits the inherent predictability of X-ray absorption in planetary atmospheres. Although SEXTANT demonstrated 10 km accuracy in low Earth orbit aboard the ISS, it is expected that the performance of XNAV will improve in deep space.² As shown in this paper, HCNM only operates in orbit around planets and can achieve in-track accuracies well below 10 km. Results from the two NICER horizon crossings show that HCNM can provide in-track navigational information of < 3 km in all energy bands considered from 1-5 keV, depending on a source's brightness. Our method of error analysis correctly identifies a suitable range of confidence for HCNM results and successfully encapsulates the benefits of source brightness. Because photoelectric cross section varies strongly with energy, it is necessary to divide the data into energy bands and determine navigational information from each band, but the answers can then be combined in a weighted mean. A weighted mean of results from all energy bands shows that HCNM is precise to about 800 m with V4641 Sgr. and 170 m with the Crab Nebula, which is about 20 times brighter than V4641 Sgr. in X-rays. The case study presented in this paper of an atmosphere with uncertainty in atmospheric composition also provides a baseline understanding of the *error budget* of HCNM in a deep space navigational scenario when there are uncertainties in a planet's atmospheric model.

ACKNOWLEDGMENTS

We would like to thank Satoru Katsuda for valuable discussions and important cross-checks on our methods of analyzing horizon crossings. We would also like to thank Kevin D. Anderson of the University of Maryland, and Campbell T.L. Dunham and Suneel I. Sheikh of ASTER Labs, Inc. for their efforts to integrate HCNM into their navigational Kalman Filter.

We would like to thank Keith Gendreau, Zaven Arzoumanian, and others on the NICER team for all of their efforts to observe horizon crossings with NICER. They have had to work very hard and try many times in order to achieve the horizon crossing presented in this paper, and without their efforts, HCNM would not be possible.

NICER research performed at NRL is supported by NASA.

APPENDIX A: INPUTS TO THE NRLMSISE-00 DENSITY MODEL

We access the NRLMSISE-00 atmospheric model through “pymis”, a python wrapper for the MSIS model, created by Greg Lucas and the University of Colorado Space Weather Technology, Research and Education Center (SWx TREC). Table 7 shows the inputs to NRLMSISE-00 when extracting the density profiles used in this paper.

Table 7: Inputs to the MSISE-00 atmospheric model to extract profiles of density as a function of altitude. Longitude and Latitude correspond to the “graze point” (gp), the point on the telescopic line of sight where tangent altitude equals zero, which is shown in Figure 1. Geomagnetic Ap indices are provided by GFZ German Research Centre for Geosciences.²¹ The f10.7 cm solar flux is provided by Space Weather Canada (1 sfu = 10^4 Jy).

Observation	$t_{0,mkf}$ (UTC)	Lat. of gp	Lon. of gp	F10.7 (sfu)	Ap
V4641 Sgr	2020-02-03 19:39:27.25	-43.26°	90.28°	69.7	12
Crab Nebula	2021-08-11 16:31:19.01	-43.91°	168.69°	75.2	2

APPENDIX B: ADDITIONAL INFORMATION

Table 8: Right ascension, declination, and out-of orbital plane angle (ψ) of the black hole binary V4641 Sgr and the Crab Nebula. The position of the ISS at the start of the horizon crossing, $\mathbf{r}_{0,mkf}$, is given in terms of latitude, longitude, and altitude.

Observation	Source RA	Source DEC	Source ψ	Lat. ISS	Lon. ISS	Alt. ISS
V4641 Sgr	274.839°	-25.407°	-2.59°	-29.53°	71.47°	424.27 km
Crab Nebula	83.633°	22.014°	2.06°	-51.38°	139.92°	436.72 km

REFERENCES

- ¹ J. R. Guinn, S. Bhaskaran, T. A. Ely, B. M. Kennedy, T. J. Martin-Mur, R. S. Park, J. E. Riedel, D. C. Roth, and A. T. Vaughan, “The Deep Space Positioning System (DPS)-navigator concept for the Lunar Gateway,” 2019.
- ² J. W. Mitchell, L. B. Winternitz, M. A. Hassouneh, S. R. Price, S. R. Semper, W. H. Yu, P. S. Ray, M. T. Wolf, M. Kerr, K. S. Wood, *et al.*, “SEXTANT X-ray pulsar navigation demonstration: initial on-orbit results,” *Proceedings of the AAS Guidance, Navigation, and Control Conference, Paper AAS 18-155*, 2018.
- ³ L. M. Winternitz, K. C. Gendreau, M. Hassouneh, J. W. Mitchell, W. H. Fong, W.-T. Lee, F. Gavril, and Z. Arzoumanian, “The role of X-rays in future space navigation and communication,” *Proceedings of the AAS Guidance, Navigation, and Control Conference, Paper AAS 13-082*, 2013.
- ⁴ J. R. Determan, S. A. Budzien, M. P. Kowalski, M. N. Lovellette, P. S. Ray, M. T. Wolff, K. S. Wood, L. Titarchuk, and R. Bandyopadhyay, “Measuring atmospheric density with X-ray occultation sounding,” *Journal of Geophysical Research (Space Physics)*, Vol. 112, June 2007, p. A06323, doi: 10.1029/2006JA012014.
- ⁵ P. B. Hays and R. G. Roble, “Stellar spectra and atmospheric composition,” *Journal of Atmospheric Sciences*, Vol. 25, No. 6, 1968, pp. 1141–1153.
- ⁶ R. G. Roble and P. Hays, “A technique for recovering the vertical number density profile of atmospheric gases from planetary occultation data,” *Planetary and Space Science*, Vol. 20, No. 10, 1972, pp. 1727–1744.
- ⁷ K. S. Wood and P. S. Ray, “The NRL Program in X-ray Navigation,” *arXiv e-prints*, Dec. 2017, doi: arXiv:1712.03832.
- ⁸ S. Katsuda, H. Fujiwara, Y. Ishisaki, M. Yoshitomo, K. Mori, Y. Motizuki, K. Sato, M. S. Tashiro, and Y. Terada, “New Measurement of the Vertical Atmospheric Density Profile From Occultations of the Crab Nebula With X-Ray Astronomy Satellites Suzaku and Hitomi,” *Journal of Geophysical Research: Space Physics*, Vol. 126, No. 4, 2021.
- ⁹ A. Rahmati, D. Larson, T. Cravens, R. Lillis, C. Lee, and P. Dunn, “MAVEN SEP Observations of Scorpius X-1 X-Rays at Mars: A Midatmosphere Occultation Analysis Technique,” *Geophysical Research Letters*, Vol. 47, No. 21, 2020, p. e2020GL088927, 10.1029/2020GL088927.
- ¹⁰ K. S. Wood, J. R. Determan, P. S. Ray, M. T. Wolff, S. A. Budzien, M. N. Lovellette, and L. Titarchuk, “Using the unconventional stellar aspect (USA) experiment on ARGOS to determine atmospheric parameters by x-ray occultation,” *Optical Spectroscopic Techniques, Remote Sensing, and Instrumentation for Atmospheric and Space Research IV* (A. M. Larar and M. G. Mlynchak, eds.), Vol. 4485 of *Society of Photo-Optical Instrumentation Engineers (SPIE) Conference Series*, Jan. 2002, pp. 258–265, doi: 10.1117/12.454259.
- ¹¹ K. S. Wood, “Navigation studies utilizing the NRL-801 experiment and the ARGOS satellite,” *Small Satellite Technology and Applications III* (B. J. Horais, ed.), Vol. 1940 of *Society of Photo-Optical Instrumentation Engineers (SPIE) Conference Series*, Sept. 1993, pp. 105–116, doi: 10.1117/12.156637.
- ¹² S. I. Sheikh, D. J. Pines, P. S. Ray, K. S. Wood, M. N. Lovellette, and M. T. Wolff, “Spacecraft navigation using X-ray pulsars,” *Journal of Guidance, Control, and Dynamics*, Vol. 29, No. 1, 2006, pp. 49–63, doi: 10.2514/1.13331.
- ¹³ K. S. Wood, P. S. Ray, M. T. Wolff, and K. Gendreau, “Satellite Navigation using X-ray Pulsars and Horizon Crossings of X-ray Stars,” *Proceedings of the AAS Guidance, Navigation, and Control Conference, Paper AAS 20-124*, 2020.
- ¹⁴ P. S. Ray, K. S. Wood, and M. T. Wolff, “Characterization of pulsar sources for x-ray navigation,” *arXiv:1711.08507*, 2017.
- ¹⁵ P. S. Ray, S. I. Sheikh, P. H. Graven, M. T. Wolff, K. S. Wood, and K. C. Gendreau, “Deep space navigation using celestial X-ray sources,” *Proceedings of the 2008 National Technical Meeting of The Institute of Navigation*, 2008, pp. 101–109.
- ¹⁶ K. C. Gendreau, Z. Arzoumanian, P. W. Adkins, C. L. Albert, J. F. Anders, A. T. Aylward, C. L. Baker, E. R. Balsamo, W. A. Bamford, S. S. Benegalrao, *et al.*, “The neutron star interior composition explorer (NICER): design and development,” *Space telescopes and instrumentation 2016: Ultra-violet to gamma ray*, Vol. 9905, International Society for Optics and Photonics, 2016, p. 99051H, doi: 10.1117/12.2231718.
- ¹⁷ M. Balucinska-Church and D. McCammon, “Photoelectric absorption cross sections with variable abundances,” *The Astrophysical Journal*, Vol. 400, 1992, p. 699, doi: 10.1086/172032.
- ¹⁸ M. J. Berger and J. Hubbell, “XCOM: Photon cross sections on a personal computer,” tech. rep., National Bureau of Standards, Washington, DC. Center for Radiation, 1987, doi: 10.2172/6016002.

- ¹⁹ J. M. Picone, A. E. Hedin, D. P. Drob, and A. C. Aikin, "NRLMSISE-00 empirical model of the atmosphere: Statistical comparisons and scientific issues," *Journal of Geophysical Research (Space Physics)*, Vol. 107, Dec. 2002, p. 1468, doi: 10.1029/2002JA009430.
- ²⁰ J. T. Emmert, D. P. Drob, J. M. Picone, D. E. Siskind, M. Jones Jr, M. Mlynczak, P. Bernath, X. Chu, E. Doornbos, B. Funke, *et al.*, "NRLMSIS 2.0: A whole-atmosphere empirical model of temperature and neutral species densities," *Earth and Space Science*, Vol. 8, No. 3, 2021, p. e2020EA001321.
- ²¹ J. Matzka, C. Stolle, Y. Yamazaki, O. Bronkalla, and A. Morschhauser, "The geomagnetic Kp index and derived indices of geomagnetic activity," *Space Weather*, Vol. 19, No. 5, 2021, p. e2020SW002641.